Journal of Theoretical Biology 529 (2021) 110856

Contents lists available at ScienceDirect

Journal of Theoretical Biology

journal homepage: www.elsevier.com/locate/yjtbi

Review

Arterial blood stealing as a mechanism of negative BOLD response: From the steady-flow with nonlinear phase separation to a windkessel-based model

Alejandro Suarez [a], Pedro A. Valdes-Hernandez [a,b], Arash Moshkforoush [a], Nikolaos Tsoukias [a], Jorge Riera [a,*]

[a] Department of Biomedical Engineering, Florida International University, Miami, FL, United States
[b] Department of Community Dentistry and Behavioral Science, University of Florida, United States

ARTICLE INFO

Article history:
Received 14 November 2020
Revised 22 June 2021
Accepted 1 August 2021
Available online 4 August 2021

Keywords:
Hemodynamics
Microcirculation
Hyperemic response
Biophysical models
CBF
Neurovascular coupling

ABSTRACT

Blood Oxygen Level Dependent (BOLD) signal indirectly characterizes neuronal activity by measuring hemodynamic and metabolic changes in the nearby microvasculature. A deeper understanding of how localized changes in electrical, metabolic and hemodynamic factors translate into a BOLD signal is crucial for the interpretation of functional brain imaging techniques. While positive BOLD responses (PBR) are widely considered to be linked with neuronal activation, the origins of negative BOLD responses (NBR) have remained largely unknown. As NBRs are sometimes observed in close proximity of regions with PBR, a blood "stealing" effect, i.e., redirection of blood from a passive periphery to the area with high neuronal activity, has been postulated. In this study, we used the Hagen-Poiseuille equation to model hemodynamics in an idealized microvascular network that account for the particulate nature of blood and nonlinearities arising from the red blood cell (RBC) distribution (i.e., the Fåhraeus, Fåhraeus-Lindqvist and the phase separation effects). Using this detailed model, we evaluate determinants driving this "stealing" effect in a microvascular network with geometric parameters within physiological ranges. Model simulations predict that during localized cerebral blood flow (CBF) increases due to neuronal activation—hyperemic response, blood from surrounding vessels is reallocated towards the activated region. This stealing effect depended on the resistance of the microvasculature and the uneven distribution of RBCs at vessel bifurcations. A parsimonious model consisting of two-connected windkessel regions sharing a supplying artery was proposed to simulate the stealing effect with a minimum number of parameters. Comparison with the detailed model showed that the parsimonious model can reproduce the observed response for hematocrit values within the physiological range for different species. Our novel parsimonious model promise to be of use for statistical inference (top-down analysis) from direct blood flow measurements (e.g., arterial spin labeling and laser Doppler/Speckle flowmetry), and when combined with theoretical models for oxygen extraction/diffusion will help account for some types of NBRs.

Contents

* Corresponding author at: FIU Engineering Center, 10555 West Flagler St, EC 2678, Miami, FL 33174, United States.
E-mail address: jrieradi@fiu.edu (J. Riera).

https://doi.org/10.1016/j.jtbi.2021.110856
0022-5193/

1. Introduction

The blood-oxygen-level dependent (BOLD) contrast constitutes the foundation for the most popular neuroimaging modality to study neuronal activity, i.e., functional magnetic resonance imaging (fMRI). A typical BOLD response comprises an initial dip (*absent sometimes*), a positive rise that peaks ~3–5 s after the stimulus onset, and a post-stimulus overshoot (Ogawa et al., 1998). The positive peak is associated with an increase in cerebral perfusion due to vessel dilation, namely the functional hyperemic response. As many experiments linked these vasodilations to neuronally-triggered vasoactive mechanisms (Riera and Sumiyoshi, 2010), the positive BOLD response has become a widely used neuroimaging modality in the community to study brain activity in normal (Rosen et al., 1998) and pathological conditions (Matthews et al., 2006). The discovery of a negative BOLD response (NBR) almost two decades ago by Shmuel et al. (2002), has slowed down further progress in the field, as its link to neuronal activation remains elusive. Understanding the physiological mechanisms underlying the NBR has been the focus of attention of many research groups.

The most accepted mechanism for NBR is neuronal deactivation due to either local (Shmuel et al. 2002; Boorman et al., 2010; Maggioni et al. 2016) or remote inhibition (Boorman et al., 2010; Klingner et al., 2010; Schäfer et al. 2012). NBRs due to neural inhibition have also been associated to the deactivation of default mode network (Raichle et al., 2001; Gusnard and Raichle, 2001). A mechanistic model linked to this neuronal inhibition hypothesis for NBR has been recently proposed (Sten et al., 2017). An increase in oxygen demand in an activated region without the necessary blood supply constitutes another possible mechanism of NBR. Such a neurovascular/metabolic decoupling has been reported in normal (Devor et al., 2008; Schridde et al., 2008; Nagaoka et al., 2006) and preclinical (Song et al., 2016) animal studies. Based on recent findings of regional decrease in cerebral blood flow (CBF), together with an unexpected increase in cerebral blood volume (CBV) (Goense et al. 2012), Bandettini (2012) suggested a back pressure phenomenon from venous compartment as a potential mechanism underlying NBR. Goense et al. (2012) findings are in line with 2-P microscopy data from behaving mice showing large increases of venous diameter in motor areas for which arteriole diameter apparently decreases (Patrick Drew, *personal communication*). NBR has also been linked to a decrease in CBV, induced by endogenous neurotransmission (Shih et al., 2009).

An alternative—purely vascular in nature—mechanism for an NBR, was put forth by Harel et al. (2002), soon after the discovery of the phenomenon. The authors suggested that reallocation of cortical blood resources from the nearby penetrating vasculature might occur to meet local metabolic demand in areas with increased neural activity, a phenomenon termed arterial blood stealing (ABS). This hypothesis was strongly refuted by Smith et al. (2004) based on experimental data from five healthy adults. Despite that, another independent study (Kannurpatti and Biswal, 2004) supported the hypothesis in the same year. More recently, two experimental studies in rats (Hu and Huang, 2015) and cats (Ma et al., 2017) also provided substantial evidence for a non-neuronal origin for the NBR and directly suggested the possibility of a vascular blood stealing. Yet, an issue that remains unclear is whether blood stealing from arterioles sharing the same blood-feeding artery is feasible from a fluid dynamics perspective, given normal physiological compositions of suspended hematocrit (Hct) in blood vessels. A preliminary theoretical work by Boas et al. (2008) suggested that blood stealing was possible in vessels surrounding a brain area undergoing a hyperemic response. However, this study did not take into account the dynamics of red blood cells (RBCs) at vessel bifurcations (phase-separation) and the effect of changes in the hematocrit, and thus the viscosity, with vessel diameter (Fåhraeus, Fåhraeus-Lindqvist effect). Detailed computational models of incompressible/laminar fluid dynamics are helpful to explore further the blood-stealing hypothesis. The use of such a theoretical approach might also help finding simplified parametric representations to phenomenologically model the NBR and other types of CBF observations, as well as to design experimental paradigms to determine circumstances under which ABS occurs in the brain vasculature.

In this paper, we investigate whether ABS is a feasible phenomenon in the cortical vasculature by performing simulations in an idealized microvascular network upon dilating an arteriolar segment. Simulations are based on established physical principles (Hagen-Poiseuille equation) and account for nonlinearities in hemorheology observed in-vivo (i.e., the Fåhraeus, Fåhraeus-Lindqvist and the phase separation effects; Pries and Secomb, 2008). Furthermore, we investigate how changes in vascular parameters affect the ABS phenomenon, i.e., basal hematocrit, inlet pressure, the length of arterioles, and resting diameter of arterioles. The detailed model is highly complex with approximately dozens of equations and five state variables per segment. For the present study, we had to solve a linear system of 36 algebraic equations to obtain the CBFs (Q) and drop pressures (ΔP) in the 22 vessel segments of the idealized microvascular network used in this study. These state variables were then inserted into 66 (22×3) equations to finally estimate the other three state variables (hematocrit – H, resistance – R, and viscosity – η) in each vessel segment. Therefore, the problem quickly scale-up for more complex/branchy microvascular network. In previous literature, parsimonious hemodynamic models of a local (e.g., voxel) microvascular network have been useful to reduce the complexity and to make statistical inference feasible (Riera et al., 2007). Here, we proposed a compartmental model based on empirical relationships combining two regions modelled as windkessels (Mandeville et al., 1999) connected to the same feeding artery. We included a solenoid to account for the inertial forces of the fluid upon dilating an arteriole. We demonstrated that simulation results obtained from our detailed fluid dynamics model, for a range of physiological hematocrit percentages, can be successfully fitted by the parsimonious windkessel-based model upon optimizing selected parameter values. Although the ABS hypothesis was motivated from BOLD signal

observations, our study only focuses on the mechanisms for hemodynamic/RBC changes. In a recent study (Suarez et al., 2021), we have used our theoretical framework to model NBR in epilepsy.

2. Methods

This section is divided into two subsections: 2.1) Biophysical modeling and 2.2) Simulated data analysis. Both the detailed and parsimonious models are described in subsection 2.1, which includes the main hypotheses underlying the model and the final equations/parameters. Sub-section 2.2 presents the methods used for the analysis of the simulated data: (a) a global sensitivity analysis of certain parameters of the detailed fluid dynamics model and (b) the strategy for estimation of equivalent parameters in the parsimonious windkessel-based model.

2.1. Biophysical modeling

To formulate a *detailed fluid dynamics model* for blood flow with RBCs suspension, an idealized microvasculature network must be created. Inspired by the work of Boas et al. (2008), a simplified symmetric microvascular network was used in this study (Fig. 1), with a similar vessel branching structure and the same diameter range. This microvasculature network is consistent with experimental data from rodents and cats (Gagnon et al., 2015). In combination with steady-state equations for laminar flow and empirical formulations accounting for the nonlinearities arising from the non-continuum nature of blood, the idealized vascular network was utilized to model the global vessel responses to a localized vasodilation in small parenchymal arterioles. This theoretical framework allows the evaluation of the dependencies of the stealing phenomenon with basal hematocrit within the physiological range for the human brain (Yang et al., 2015); the inlet pressure of the network, which can be interpreted as resistive changes upstring in the macro-vasculature; and both length and diameter of the feeding and daughter arterioles. The network was defined by a combination of vessel segments and bifurcation nodes. At each node, the feeding higher-order arteriole with a greater diameter bifurcates into two lower-order daughter arterioles with smaller diameters. The arterioles further extend into the capillaries (segments with the smallest diameter) before converging into draining venules. The inlet and outlet nodes represent a large pial artery and vein, respectively. The pressures at the inlet (Artery) and outlet (Vein) nodes were kept constant (Boas et al., 2008). Parameters for the microvascular network and the ranges for the evaluated parameters are listed in Table 1.

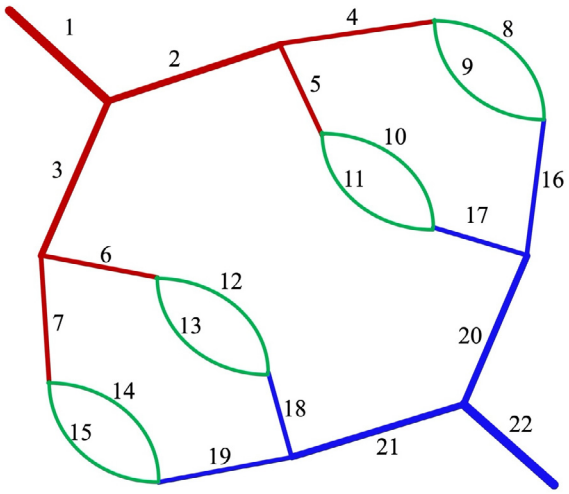

Fig. 1. The microvascular network: arterioles (red), capillaries (green), and venules (blue). Numbers [1 – 22] denote segments.

Table 1
Physiological parameters and boundary conditions of the microvascular network.

Diameters (μm)		Lengths (μm)	
1st order arteriole	27.5	1st order arteriole	100
2nd order arterioles (feeding $\boldsymbol{D_F}$)	17.5 [15.5,19.5]	2nd order arterioles (feeding $\boldsymbol{L_F}$)	100 [70,130]
3rd order arterioles (daughters $\boldsymbol{D_D}$)	11 [10,12]	3rd order arterioles (daughters $\boldsymbol{L_D}$)	100 [70,130]
Capillaries	8	Capillaries	250
3rd order venules	13	3rd order venules	100
2nd order venules	19.5	2nd order venules	100
1st order venule	33	1st order venule	100
Boundary conditions			
Inlet arteriole pressure ($\boldsymbol{P_A}$)		60 [50,70] mmHg	
Outlet venule pressure (P_V)		25 mmHg	
Basal hematocrit ($\boldsymbol{H_0}$)		0.45 [0.32, 0.50]	

Note: Ranges provided are within physiological range and were used to study their effect on the stealing. In this table, bold case is used to show parameters with a known range of values.

All equations used in the detailed fluid dynamics model, the hypotheses underlying these equations, and the references where they were originally proposed are presented in Appendix A. A flow-chart describing state variables dependency and boundary conditions in our detailed fluid dynamics model is shown in Fig. 2.

To characterize the stealing phenomenon, we defined the stealing percent/ratio as $\rho_{steal} = [(1 - min(Q_p(t)))/\ (max(Q_a(t)) - 1)] * 100\%$, which quantifies the relationship between the maximum absolute value of CBF decrease in the passive arteriole $Q_p(t)$ and the CBF increase in the actively-dilated arteriole $Q_a(t)$.

In order to make statistical inference from actual mesoscopic data (e.g., local CBF and BOLD), a *parsimonious windkessel-based model* was formulated/validated, and specific parameters were adjusted to the detailed fluid dynamics model. The model consists of two windkessel regions connected with the same feeding artery and draining vein as shown in the equivalent electric diagram (Fig. 3). The model consists of three differential equations per brain region, including values of the relative CBF (f_a), the delayed vessel compliance (a) and the relative CBV (v). We also included a solenoid to account for the inertial forces of the fluid (Spronck et al., 2012). The details about this model are presented in Appendix B. Equations, state variables, and parameters are presented in tables which their respective reference source. Windkessel models have been very useful to phenomenological explain CBF and BOLD signal

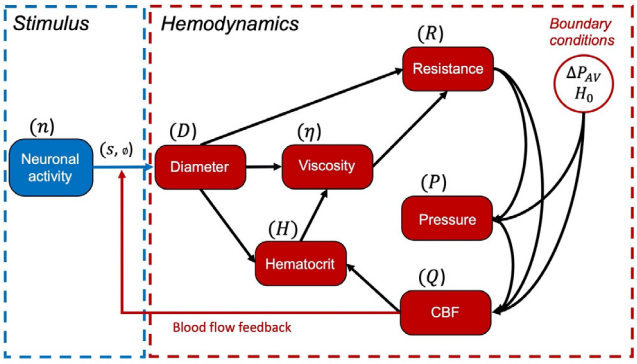

Fig. 2. Flow-chart for dependency of components of the flow-based model. Black arrows denote the direction of the iterative process, state variables appear within brackets, and boundary conditions are inside the red circumference. The red section represents the iterative process of hemodynamic response, and the blue section represents the stimulation. Red arrow represents a feedback that set the saturation limit of blood flow increase.

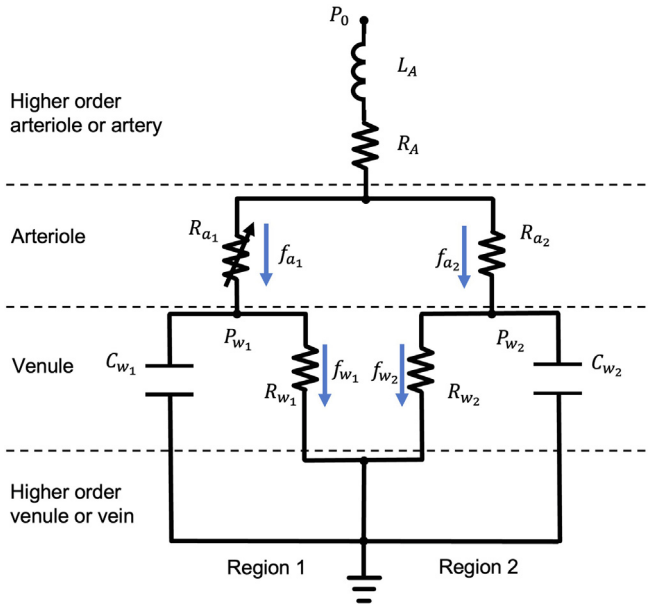

Fig. 3. Electrical circuit of the windkessel-based model. Two windkessel regions are connected to the same higher order arteriole, which is represented with a resistor (R_A) and a solenoid (L_A) to account for the inertial forces. The inlet pressure (P_0), windkessel pressure (P_{wi}), arteriole resistances (R_{ai}), windkessel resistances (R_{wi}), and compliances (capacitors, C_{wi}) are also shown. Relative flows in (f_{ai}) and out (f_{wi}) of each windkessel region and their respective direction are represented using blue arrows. Doted lines separate different compartments of the model.

in both basic research (Riera et al., 2007) and clinical practice (Suarez et al., 2021). Hence, we believe our extension of the windkessel theoretical framework to account for ABS due to hematocrit and nonlinear vascular effect at a mesoscopic scale will be very useful to explain some types of NBRs.

2.2. Simulated data analysis

2.2.1. Sensitivity analysis – detailed fluid dynamics model

A global sensitivity analysis was performed to assess the sensitivity of stealing percent/ratio to variation in certain physiological parameters of the network, i.e., inlet hematocrit, inlet pressure, length and diameter of the feeding arteriole, length and diameter off the daughter arterioles. Each parameter was allowed to vary within their physiological range (Table 1). We used Latin hypercube sampling (LHS) method with uniform distribution to select 1000 random parameter sets to perform the sensitivity analysis (Moshkforoush et al., 2021). The detailed fluid dynamics model was solved for each parameter set in the microvascular network and the stealing percent/ratio was then calculated. The partial rank correlation coefficient (PRCC) for each parameter was then computed to determine the magnitude of the parameter influence (positive or negative) on the stealing. A 95% confidence interval was chosen to determine if the exerted influence is statistically significant.

2.2.2. Parameter estimation – parsimonious windkessel-based model

Multiple realizations of CBF variations (Eq. A5) at the two segments (active arteriole – $Q_a(t)$, passive arteriole – $Q_p(t)$) of the bifurcating penetrating arteriole were generated using the detailed fluid dynamics mode upon a neuronally-induced vasodilation of the active arteriole, named simulated data. An additive Gaussian white noise was introduced to represent instrumental errors in CBF measurements. We then performed parameter estimation of the parsimonious windkessel-based model to fit the simulated data via minimization of the following optimization function at discrete time instants t_k:

$$F_{opt}\left(R_A, R_a^0\right) = \frac{1}{N}\sum_{k=1}^{N}\left[\left(Q_a(t_k) - f_{a_1}\left(t_k; R_A, R_a^0\right)\right)^2 + \left(Q_p(t_k) - f_{a_2}\left(t_k; R_A, R_a^0\right)\right)^2\right]$$

where F_{opt} is optimization function, N is number of time steps in the data, k is the time step index. The parameter (R_A, R_a^0) estimation was performed by finding the global minima of the optimization function using MATLAB's function *fmincon*.

3. Results

3.1. Evaluation of the ABS phenomenon using the detailed fluid dynamics model

Relative changes in CBF in both active and passive vessel segments (arterioles), originating from the same bifurcation (Fig. 4A), were obtained in response to an assumed increase in the relative neuronal activity (the green trace) in the active segment, which resulted in a relative change of ~30% in the diameter of the active arteriole (segment 4) (Fig. 4B). Fig. 4C illustrates an increase in the CBF in the active region (segment 4) as opposed to an apparent decline in the passive segment (segment 5), suggesting a stealing effect. The black dotted lines represent CBF changes when the discharge hematocrit was kept constant in each vessel (Fig. 4D), indicating that in the absence of changes in hematocrit in the daughter arterioles, the ABS effect is almost completely abolished. Thus, model simulations suggest that the presence of ABS in our network is primarily attributed to an increase in hematocrit in the passive arteriole, likely due to the phase separation effect (Pries and Secomb, 2008). The rise in the hematocrits results in an increase in the apparent viscosity (Fig. 4E), and subsequently, the CBF resistance. The blood viscosity in the active arteriole, however, showed a substantial decline upon vessel dilation, and also with hematocrit decreasing (Fig. 4F), contributing to the drop in the vessel's resistance to CBF. Nonetheless, the decrease in resistance is primarily caused by vessel dilation, as diameter has the highest contribution in the overall flow resistance (Eq. A5).

We next evaluated the dependency of the observed ABS effect to a) basal hematocrit (H_0) (Fig. 5A), b) inlet pressure (P_A) (Fig. 5B), c) the length of the feeding arterioles (L_F) (Fig. 5C), d) the length of the daughter arterioles (L_D) (Fig. 5D), e) the resting diameter of the feeding arterioles (D_F) (Fig. 5E), and f) the resting diameter of the daughter arterioles (D_D) (Fig. 5F). All these parameters were varied within the range provided in Table 1. Changes in basal hematocrit caused changes in stealing percent that ranged from 27.4% (H_0 = 0.32) to 23.3% (H_0 = 0.50) (Fig. 5A). Fig. 5B shows no variations in the CBF in both passive and active regions after changes in the inlet pressure. We observed an increase in the stealing percent/ratio with increasing the resting diameter of the daughter arterioles (Fig. 5F, from 14% – $D_D = 10\mu m$ to 37% – $D_D = 12\mu m$) as well as increasing the length of the feeding arterioles (Fig. 5C, from 24.8% – $L_F = 70\mu m$ to 25.6% – $L_F = 130\mu m$), this last being very small. On the other hand, increasing the length of the daughter arterioles (Fig. 5D) and increasing the resting diameter of the feeding arterioles (Fig. 5E) caused a decrease in the stealing percent/ratio from 35% % ($L_D = 70\mu m$) to 17.6% ($L_D = 130\mu m$) and from 28.1 ($D_F = 15.5\mu m$) to 23.2% ($D_F = 19.5\mu m$), respectively. These results show the inverse effect of length and diameter on the resistance (Eq. A5). These results were theoretically corroborated by means of the global sensitivity analysis. The PRCC for each parameter is shown in Fig. 5G. Changes in basal hematocrit, length

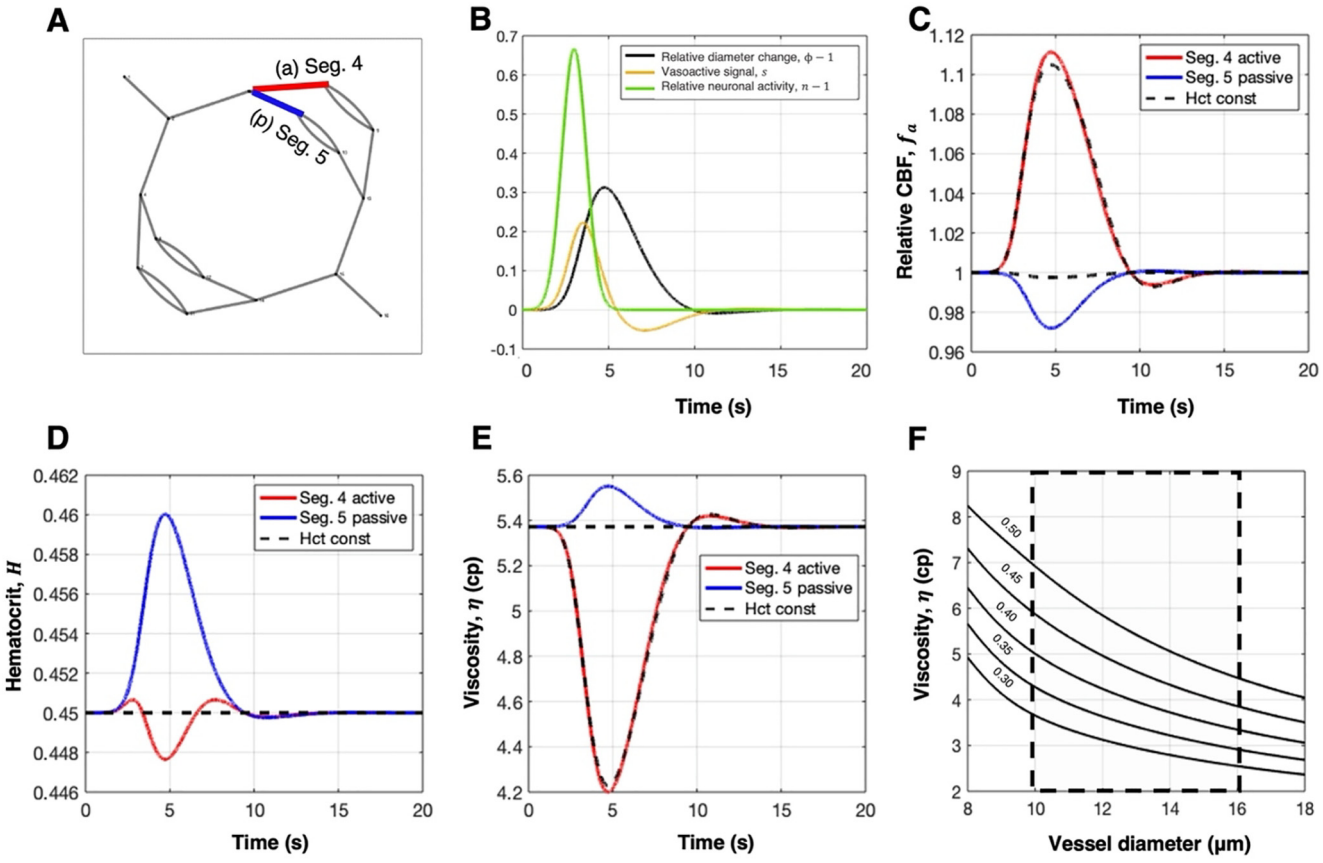

Fig. 4. Arterial blood stealing – simulations performed with the detailed flow dynamics model. A) Highlighting the two observed vessel segments (actively-dilated (a) segment 4 in red and passively-responding (p) segment 5 in blue). B) Relative diameter changes in the active arteriole due to neuronally-evoked (n) vasoactive signaling (s), C) relative changes in blood flow. D) hematocrit, E) and viscosity during dilation of the active arteriole; *red*: active arteriole, *blue*: passive arteriole, *black dotted lines*: constant hematocrit (Hct) for both arterioles. F) Viscosity values for different hematocrit and diameters calculated using equations 1–3. Parameters of the detailed flow dynamics model are kept constant in these simulations.

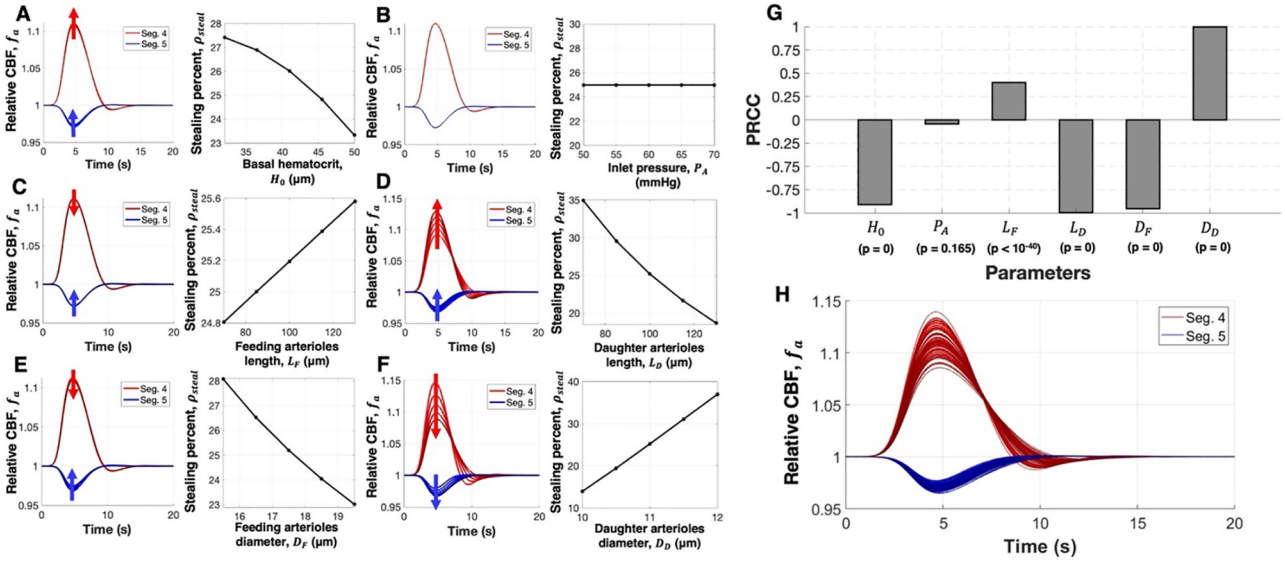

Fig. 5. Variation in the stealing phenomenon depend on physiology – simulations performed with the detailed flow dynamics model. A) Variations of basal hematocrit (H_0) within the physiological range (0.32–0.50) show small changes in CBF. B) Changes in the value of the inlet pressure (P_A) did not caused any changes in the CBF. C) Varying the length of the feeding arterioles (L_F) (Seg. 2 and 3). Stealing percent increases with length. D) Varying the length of the active arteriole (L_D) (Seg 4–7). Stealing percent/ratio decrease with length increasing. D) Varying baseline diameter (D_F) of the feeding arteriole (Seg. 2 and 3). Stealing percent/ratio decreases with vessel diameter increases. E) Varying baseline diameter of the active arteriole D_D (Seg 4–7). Stealing percent/ratio increases with vessel diameter increasing. G) Global sensitivity analysis. PRCC was calculated from 1000 parameters sets and their respective stealing ratio. PRCC equals to −1 means that changes in the parameter are maximally anticorrelated with the stealing percent; PRCC equals to 1 means that changes in the parameter are maximally correlated with the stealing percent. P-values for statistical significance are shown below each parameter. H) 100 trials of CBF simulation using randomly chosen parameter set from normal distribution within the same range shown in A-G. The stealing percent ranged from 16.4% to 40.5%.

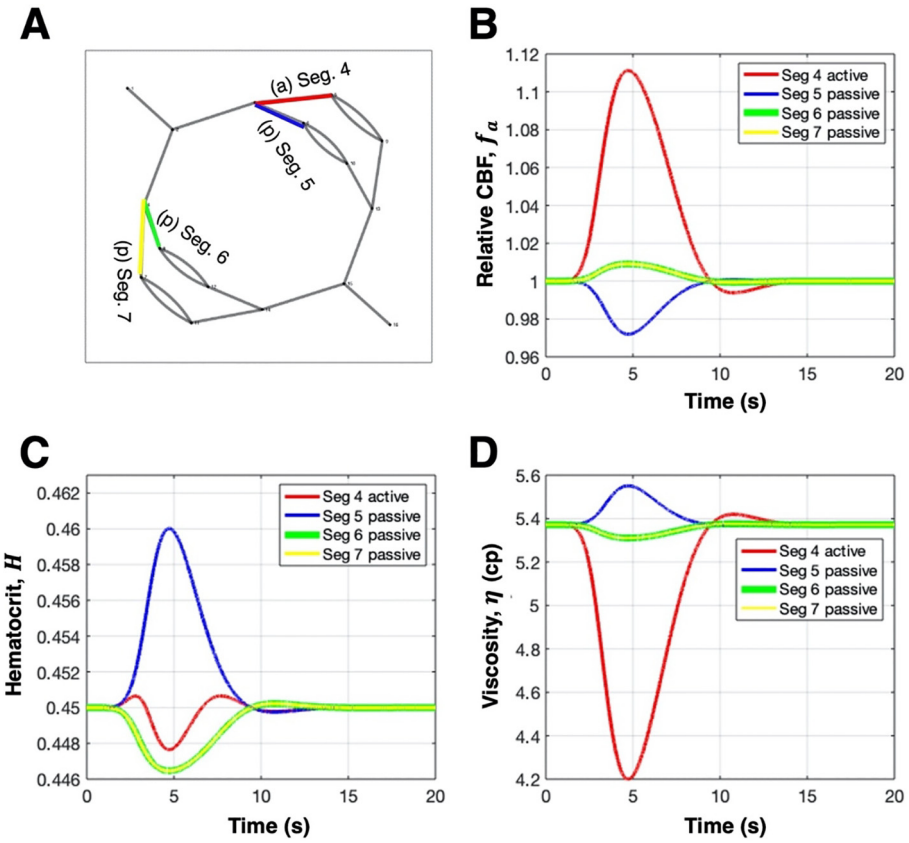

Fig. 6. Effect of the stimulation of the active arteriole on the CBF response in all 3rd order arterioles – simulations performed with the detailed flow dynamics model. A) All 3rd order arterioles are highlighted on both sides of the network. B) Small increase in CBF in segments 6 and 7 is observed in response to dilation of segment 4 arteriole. C) Decreasing hematocrit and consequently decrease in viscosity. If more hematocrit goes into the side where flow is increased, less RBCs will go into the non-stimulated side, which will result in decreasing viscosity (D), decrease in resistance, and thus increase in flow.

of the daughter arterioles, and of diameter of the feeding arterioles are anticorrelated with the stealing percent. On the contrary, changes in length of the feeding arteriole and the resting diameter of daughter arterioles are correlated to the stealing percent. There was not significant correlation found between the stealing percent and the inlet pressure. Furthermore, we modeled 100 trials randomly generating each of the parameters evaluated for each vessel using normal distribution (Fig. 5H). The maximum and minimum values obtained for the stealing percent were of 40.5% and 16.4%, respectively.

Additionally, we analyzed whether dilation of an arteriolar segment (segment 4) can result in an ABS from regions of the network that are not directly supplied by the same feeding arteriole (segments 6 and 7 in Fig. 6A). Results from Fig. 6B shows a small increase in CBF in these two 3rd order arteriolar segments (segments 6 and 7), upon dilation of the active arteriole in segment 4 (Fig. 6B). This increase is because red blood cells preferentially go in the direction of higher blood flow when both daughter vessels have the same diameter; which means that the feeding arteriole of segments 4 and 5 will get more hematocrit due to its increased flow (Fig. 6C), resulting in a decrease in viscosity in segments 6 and 7 (Fig. 6D); hence a decrease in resistance and the subsequent increase in the CBF.

3.2. Complexity reduction via a parsimonious windkessel-based model

Lastly, we examined whether the proposed parsimonious windkessel-based model on bifurcating vessels can reproduce the results obtained from our detailed fluid dynamics model for a physiological range of hematocrit percentages. A ground-truth profile, representing the blood flow distribution in segments 4 and 5 upon dilation of the vessel in segment 4, was generated using the detailed fluid dynamics model and a Gaussian noise [$N(0, \sigma^2)$, with $\sigma = 0.003$] was added to the synthesized traces to account for potential instrumental noise (simulated data, Fig. 7, *left panel*). We then fitted the noise-added ground-truth profile using the parsimonious windkessel-based model upon optimizing select parameters of the model. As illustrated in Fig. 7, the parsimonious windkessel-based model (black traces) was capable of accurately representing CBF data generated with the steady-flow model via optimizing two phenomenological parameters: 1) the resistance of the feeding 2nd order arteriole (R_A) and 2) the baseline resistance of the 3rd order bifurcating arterioles ($R_a^{(0)}$). Furthermore, we evaluated the dependency of these two parameters to hematocrit percentages in the vascular network (Fig. 7, *right*). Results show a parabolic decrease in R_A, and a parabolic increase in $R_a^{(0)}$.

4. Discussion

In this work, we performed CBF simulations in a simplified, microvascular network using a Hagen-Poiseuille-based theoretical framework to examine conditions under which ABS could occur in the neocortical vasculature. Results show that during a hyperemic response, blood from the surrounding vasculature is reallocated to the perfused vessel if they share a common feeding vessel (Fig. 4). Stealing percent/ratio was obtained to be consistent with previous experimental reports (Harel et al., 2002; Kannurpatti and Biswal, 2004; Shmuel et al., 2002). Additionally, the plasma and RBCs are

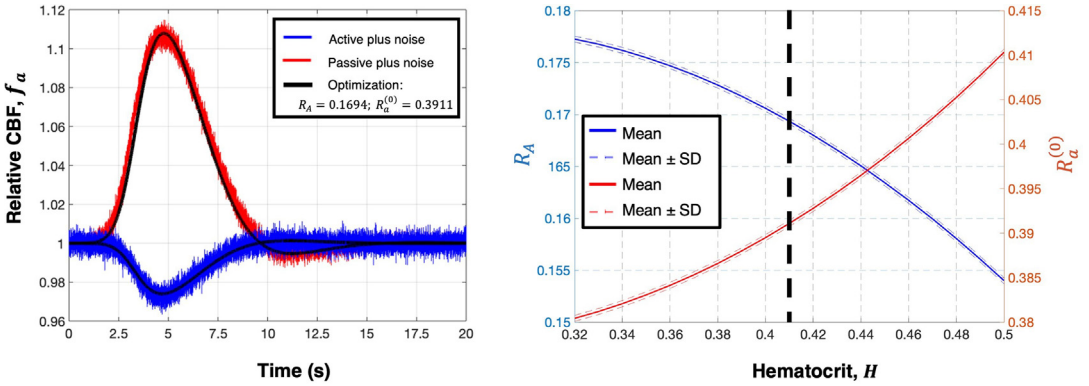

Fig. 7. Fitting of the simulated data. *Left panel*: observational data plus instrumental noise generated using the detailed flow dynamics model with hematocrit value of 0.41 (red – active segment and blue – passive segment) and the corresponding data fitting (optimization, black curve) using the parsimonious windkessel-based model. *Right panel*: Estimated parameters ($R_A, R_a^{(0)}$), solid line: mean, dotted line: standard deviation, for physiological range of hematocrit after 30 trials for each value. Black vertical dotted line represents the value of the parameters used in *left panel*.

also not equally distributed between the two daughter arterioles due to nonlinear phase separation dynamics at vessel bifurcations. The hematocrit percentage in a vessel decreases as we move away from its centerline. In contrast, plasma flows preferentially near the vessel wall. Therefore, plasma flowing near the vessel wall will easily fill the gaps created in a dilating arteriole. The associated drop in the relative hematocrit (and hence, in viscosity), together with the increase in vessel diameter, result in a noticeable decrease in the resistance of the actively dilated vessel. On the contrary, plasma refilling of a dilating arteriole occurs at a cost of reducing plasma in the surrounding "passive" vasculature, resulting in an increase of viscosity and thus, in the resistance. Interestingly, ABS seems to be related to changes in all parameters that define the resistance of both the feeding and daughter arterioles. In the absence of a vessel dilation at a bifurcation, RBCs tend to flow preferentially toward the direction of an increased blood flow. This effect can be observed as a relative decrease in viscosity in distant vessels that are not sharing a common feeding arteriole with the dilated segment (Fig. 6). We demonstrated that the relationship between the diameter of the feeding vessel and its bifurcating daughter branches play a key role in the magnitude of stealing percent/ratio. Finally, we proposed a parsimonious model based on windkessel theory to reproduce ABS observed in the detailed flow dynamics model. We fitted the changes in CBF in the active and passive arteriolar segments obtained by the steady-flow theoretical framework upon optimizing select parameters of the windkessel-based model.

4.1. Using a solenoid to parsimoniously account for flow-response inertia

The diameter of the vessels used in our simulations with the detailed flow dynamics model are relatively small (from 8 to 33 μm). However, we demonstrated that the stealing effect does not depend on the diameter of an isolated single vessel segment, but on their relative ratio of the feeding (anti-correlated) and daughter (correlated) segments. Therefore, the stealing effect can in principle occur at any vessel bifurcations within the cortex, even at the biggest pial arteries. In mice, large pial arteries could have a diameter of up to 200 μm (Qian et al., 2018). However, the diameter of vessels in the human neocortex could range from 10 μm (smallest arterioles) to 3 mm (large arteries) (Reina-De La Torre et al., 1998; Gutierrez et al., 2014), in which case the inertial time constant in the neocortex should not be neglected (Fig. 8): mice (1.4 ms) and humans (0.3 s). Time shifts (~1–5 s) between the peak of the positive hemodynamic response and that in the surrounding negativity have been reported in different studies using MRI-based (Goense et al., 2012; Harel et al., 2002; Shmuel et al., 2002, 2006) and optical-based (Hu and Huang, 2015) techniques. Based on our simulations, a blood stealing effect at a single vessel bifurcation is not likely to cause these temporal shifts. Although these shifts could in principle arise from non-vascular effects, e.g., delays in neuronal communications, there are two vascular mechanistic scenarios that could explain them: 1) the existence of nonlinear auto-regulatory mechanisms (e.g., myogenic tone) that might shift the increase/decrease of flow in any specific vascular brain region, and/or 2) an averaging effect of local, inertia-induced blood stealing in various bifurcating vessels at different time points. Also, departure from the steady-state assumptions could cause shifts in the time of these hemodynamics peaks. Exploring these hypotheses is beyond the scope of this study. However, incorporating a solenoid in the parsimonious windkessel-based model can accommodate all these effects by just introducing different inertial time constants. Note that the shift between the positive and negative CBF peaks cannot be accounted for using a solely resistive windkessel model. The typical sampling rate for an fMRI BOLD signal is 1 *s*, for which this effect in a single vessel bifurcation would not be detectable. However, our extended model can be applied to optically-based observations of CBF (e.g., laser Doppler/Speckle flowmetry), which due to their higher sampling rate (up to 64 Hz) have the resolution to detect temporal shifts caused by a

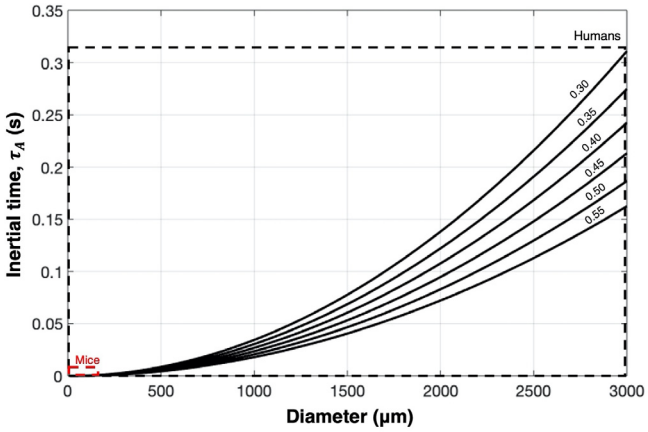

Fig. 8. Inertial time dependence to vessel diameter and hematocrit. Black numbers on the top right denotes respective hematocrit values. Doted rectangular region denote the rage of vessel diameters for two different species (*black* – human; *red* – mice).

single vessel bifurcation. Our work constitutes a proof-of-concept that the stealing phenomenon can theoretically occur even without introducing other non-linear phenomena in vessel dynamics, e.g., vessels autoregulatory processes.

4.2. Quasi-steady-flow assumption

Decrease in resistance due to vessel dilation (maximum 30%) implies the expanded region have to be refilled with blood. Our model assumes that, compared to the impulse response function of the system, the refilling is instantaneous. This assumption can be justified with several mathematical estimations that we discuss as follows. Using the conservation of mass, the time that the increased blood flow will take to fill the empty volume created by this maximum 30% dilation was about 0.5 s, which is smaller compared to the hemodynamic impulse response function (~2–3 s to reach the peak). As dilation is not happening in the passive arteriole, this assumption may have just minor implications in the shape of the negative CBF response. Also, the two main factors modifying the stealing phenomenon explored in this study, the phase separation effect and resting diameter relationship between the feeding and daughter vessels, are independent of time. Furthermore, the matching of our stealing percent/ratio with previous experimental data (Harel et al. 2002; Shmuel et al., 2002; Kannurpatti and Biswal, 2004) proved that the amplitude of the positive and negative response is less related to transient flow. In future work, we might include transient approximations in order to evaluate any potential impact. Previous studies involving transient variations in vessel diameters, venous in this case, have also assumed quasi-stationarity regime in blood refilling (Grubb et al., 1974). Most of the models for hemodynamic response have been built on the quasi-stationary relationship between CBF and CBV ($f = v^{1/\phi}$, Mandeville et al., 1999; Riera et al., 2004; Boas et al., 2008). Including a time-invariant visco-elastic effect (Zheng and Mayhew, 2009) had minor implication in the hemodynamic response function.

4.3. CBF-diameter mismatch

Our results show a ~10% maximum peak of the relative CBF in the dilated arteriole after a ~30% relative change in the vessel diameter, which is not in complete agreement with some previous theoretical and experimental work in the literature. For example, using simulations in a vascular anatomical network (VAN) model, Boas et al. (2008) reported 2.3% change in arterial CBF after changes in vessel resistance equivalent to a 15% change in diameter. A more recent study by the same group (Gagnon et al., 2015) applying the VAN theoretical framework to mice brain voxel of $600 \times 600 \times 600\mu$ m (real network) reported 25% increase in CBF for a 10% change in vessel diameters. The proposed 10% change in diameter was based on experimental measurements with two-photon microscopy. As we used similar physiological parameters in our simulations, we were expecting comparable relative CBF changes in our results. To obtain the CBF distribution, the VAN model combines an equivalent electrical circuit with two resistors per each vessel segment and the windkessel theory. Each vessel resistance and flow were computed using the Hagen-Poiseuille equation. However, they did not consider the dynamics of RBCs at vessel bifurcations (the phase separation effect), nor did they account for changes in blood apparent viscosity with vessel diameter (Fig. 4F). An experimental study (Driscoll et al., 2013) reported an increase in perfusion of about 100% for a 40% diameter change in rats undergoing a forelimb stimulation paradigm. However, CBF was indirectly estimated using a time/space approach to determine RBCs velocity from contrast-image streaks using two-photon laser scanning microscopy. The diameters were simultaneously measured using two-photon microscopy upon a tail injection of a fluorescent dye. Their results were based on some considerations regarding the blood velocity profile and homogeneity of RBC size that could introduce uncertainties in the reported values. The simplicity and symmetry of our network, alongside with the fact that we imposed a constant pressure difference between the inlet and the outlet nodes, allows for pressure reconfiguration in response to a resistance drop at the dilated arteriole. Furthermore, previously mentioned reports of CBF changes were based on the dilation of a larger number of arterioles and more complex vascular network structures, which may be another explanation for the CBF-diameter mismatch. This work is mainly focused on CBF changes after dilating only one specific small arteriole in order to provide a proof-of-concept for the blood stealing effect. The future use of larger and more realistic microvasculature with vessel dilation in an extended region might result in diameter-CBF relationships consistent with those proposed in previous studies.

4.4. Interspecies variability

Studies involving hemodynamics changes linked to CBF stealing in brain vasculature have been performed among different animal species. Kannurpatti and Biswal (2004) performed CBF measurements using laser doppler imaging (LDI) in the rat somatosensory cortex during whisker stimulation. Similarly, Hu and Huang (2015) combined optical imaging and electrophysiology to study positive and negative hemodynamic responses (PHR/NHR) in the rat cortex during hindlimb electrical stimulation. In cats, Harel et al. (2002) studied BOLD and CBV signal changes in the occipital lobe in response to visual stimulation using T2*-weighted fMRI of 4.7-T. Also, Ma et al. (2017) measured CBV and blood oxygenation changes related to the nearby neuronal activity in the visual cortex of cats. In the latter, hemodynamics measurements were obtained using intrinsic signal optical imaging (ISOI), while neuronal activity was characterized by combining planar and laminar electrophysiological recordings. As these studies were performed in cats and rodents, we built our microvascular network consistent with physiological data from these species (Boas et al., 2008, Gagnon et al., 2015). However, variations in the CBF stealing effect can result from interspecies variability in vessel network anatomy and hematocrit.

Basal hematocrit constitutes a source of variability, as our results indicated (Fig. 5B and 5G). Negative changes in CBF in the passive arteriole are mainly caused by hematocrit variations in response to the dilation of the active arteriole. In this work, we used a basal hematocrit range from the human brain, ranging from 0.32 to 0.50 (Kiyohara et al., 1985). In the case of mice, brain hematocrit ranges from 0.15 to 0.55 (Lyons et al., 2016), which will imply a small increase in the stealing percent/ratio for the range of values from 0.15 to 0.32 and a small decrease for the range of values between 0.50 and 0.55. Normal brain hematocrit levels in cats range from 0.20 to 0.45 (Bentzer and Grände, 2017; de Courten-Myers et al., 1985; Muizelaar et al. 1992); thus, we expect a small increase in the stealing percent/ratio for values from 0.20 to 0.32. Differences in cerebral microvascular complexity between mice and humans are not marked, since both vascular networks share very similar topological parameters (Smith et al., 2019). As pointed out by Smith et al. (2019), small differences in complexity could be reduced by the use of a simple scaling factor, which means that these discrepancies are mostly based on vessel diameters and lengths. Although the arteriole length only impacts blood resistance linearly (Eq. A5), it impacts the stealing phenomenon as much as arteriole diameter (Fig. 5C-G), which is powered to the fourth and is inversely proportional to resistance. This happens because the range of variation for arteriole length is much bigger

than the range of diameter (Table 1). Blood vessels within the range of diameters presented in this study are found in both species. Results show that variations in the length and diameter of either the feeding arteriole or the daughters may affect the stealing percent positively (correlated) or negatively (anti-correlated). The relationship between the length and diameter of the feeding arteriole and its bifurcating daughters will define the amount of blood stealing from one to another.

Furthermore, it is very important to highlight that the empirical relationships of apparent viscosity used in this study (Eq. A1-3) were obtained from the experimental data in cats. The thickness of the endothelial surface layer at the inner wall of the blood vessels varies among species, which demands corresponding changes to the model to account for other animal species. A more general approach to account for viscosity dynamics was presented by Pries and Secomb (2005). They introduced a correction factor based on the thickness of the endothelial surface layer of different species into a more general framework for viscosity dynamics obtained using in vitro data.

4.5. Possible impact on BOLD signal

BOLD signal does not directly depend on CBF; rather, it depends on CBV and changes in blood oxygenation (deoxyhemoglobin concentration). Therefore, in order to estimate neuronal oxygen metabolism—directly linked to neuronal activity—from BOLD signal, a fully characterization of the CBF dynamics (including ABS) is necessary. Experimental methods, such as BOLD calibration and ASL have been used to remove the CBF component from the BOLD effect (Blockley et al., 2012). However, theoretical frameworks like the parsimonious winkessel-based model offer an alternative approach. Intuitively, blood oxygen content may be affected by hematocrit variations, which have largely been sidelined in BOLD response related studies. Thus, it is necessary to pay closer attention not only to the impact of CBF on BOLD signal, but also on the interplay between tissue oxygenation and hematocrit variability as a function of the CBF. Furthermore, it is important to highlight that ABS is not the only mechanism of NBR. A recent work by our group (Suarez et al., 2021) has integrated several NBR mechanisms in a single general framework to explain abnormal BOLD responses in epilepsy.

Acknowledgements

Thanks to Dr. Timothy W. Secomb for his clarification and recommendations related to the phase separation effect. This work was supported by the National Institutes of Health (R56NS094784-01A1).

Appendix A. The detailed fluid dynamics model

The detailed fluid dynamics model is based on the following assumptions:

- A simplified symmetric microvascular consistent with experimental data from rodents and cats.
- Steady state equations for laminar flow (i.e., the Hagen-Poiseuille equation).
- A parametric model for nonlinearities in hemorheology as observed in-vivo (i.e., the Fåhraeus, Fåhraeus-Lindqvist).
- Three parametric equations for the phase separation effects (Pries and Secomb, 2008).

Table A1 summarizes all equations in the detailed fluid dynamics model, which were used to simulate changes in hemodynamic state variables in all vessel segments of the idealized microvascular network: viscosity $\eta(t)$, vessel resistance $R(t)$, blood flow $Q(t)$, across-vessel pressure difference $\Delta P(t)$, and hematocrit $H(t)$. The blood viscosity $\eta(t)$ in each segment is calculated at each time t using empirical equations (Eq. A1-3), which were obtained from in to vivo experiments in cats (Pries and Secomb, 2008). The vessel resistance of each segment is then calculated using these viscosity values via the Hagen-Poiseuille equation (Eq. A4), assuming a steady state solution for laminar flow dynamics (Navier-Stokes equations) in a cylinder (Eq. A5) of a fixed diameter. A basal discharge hematocrit $H_0(t=0)=0.45$ was set as the initial condition for all segments of the network. For this study, the diameter of the active arteriole $D^a(t)$ was allowed to vary with time; hence, a time dependency for diameter $D(t)$ was included in general. A discussion about the validity of this particular assumption is included in section 4. Parameter L represents the length of the segment. The pressure drops $\Delta P(t)$ and volumetric blood flow, $Q(t)$, in all segments must satisfy both the Ohm's law (A5) and the continuity equation (A6). A large system of algebraic equations must be

Table A1
Set of equations used for detailed fluid dynamics model simulations.

Model type	Equations	Variable	Reference
Blood viscosity in vivo	$\eta(t)=\left(1+(\eta^*_{0.45}(t)-1)\frac{(1-H(t))^{C(t)}-1}{(1-0.45)^{C(t)}-1}\left(\frac{D(t)}{D(t)-1.1}\right)^2\right)\left(\frac{D(t)}{D(t)-1.1}\right)^2$ [A1]	Viscosity	(Pries and Secomb, 2008)
	$\eta^*_{0.45}(t)=6e^{-0.085D(t)}+3.2-2.44e^{-0.06D(t)^{0.645}}$ [A2]		
	$C(t)=(0.8+e^{-0.075D(t)})\left(-1+\frac{1}{1+10^{-11}D(t)^{12}}\right)+\frac{1}{1+10^{-11}D(t)^{12}}$ [A3]		
Hagen-Poiseuille law	$R(t)=\frac{128\eta(t)L}{\pi D(t)^4}$ [A4]	Resistance	
Flow-pressure dependence	$\Delta P(t)=R(t)*Q(t)$ [A5]	CBF and Pressures	
Continuity equation	$Q_P(t)=\sum_d Q_d(t)$ [A6]	CBF	
Phase separation effect	$logit(F_H\alpha(t))=A(t)+B(t)logit\left((\frac{Q_\alpha(t)}{Q_F(t)}-X_0(t))/(1-2X_0(t))\right)$ [A7]	Hematocrit	
	Definition: $logit(x)=log\left(\frac{x}{1-x}\right)$		
	$A(t)=-13.29[(D^2_\alpha(t)/D^2_\beta-1)/(D^2_\alpha(t)/D^2_\beta+1)](1-H_F(t))/D_F$ [A8]		
	$B(t)=1+6.98(1-H_F(t))/D_F$ [A9]		
	$X_0(t)=0.964(1-H_F(t))/D_F$ [A10]		
Mass conservation	$H_\alpha(t)Q_\alpha(t)=F_H\alpha(t)*H_F(t)Q_F(t)$ [A11]		
	$H_\beta(t)Q_\beta(t)=H_F(t)Q_F(t)-H_\alpha(t)Q_\alpha(t)$ [A12]		
Neurovascular coupling	$\frac{ds(t)}{dt}=\varepsilon_{SF}(n(t)-1)-\frac{s(t)}{\tau_s}-\frac{(Q_a(t)/Q_{a0}-1)}{\tau_f}$ [A13]	Vasoactive signal	Friston et al., 2000
	$\frac{d\varnothing(t)}{dt}=l_{SF}s(t)-l_{VD}\varnothing(t)$ [A14]	Relative active diameter	Explained bellow
	$D_a(t)=D_{a0}(1+\varnothing(t))$ [A15]	Active diameter	

solved at once to estimate $Q(t)$ and $P(t)$ in all segments and nodes respectively.

We illustrate the process for the idealized microvascular network (Fig. 1). The system matrix $\mathbf{A}(t)$ in this particular case is formed as:

$$\mathbf{A}(t)=\begin{bmatrix}
1 & 0 & 0 & \cdots & & & \cdots & 0 & 1/R_1(t) & 0 & 0 & \cdots & 0 \\
0 & 1 & 0 & \cdots & & & & 0 & -1/R_2(t) & 1/R_2(t) & 0 & \cdots & 0 \\
\vdots & \vdots & \vdots & \vdots & & & & \vdots & \vdots & \vdots & \vdots & & \vdots \\
0 & 0 & 0 & \cdots & & & \cdots & 1 & 0 & 0 & 0 & \cdots & -1/R_{22}(t) \\
- & - & - & - & - & - & - & - & - & - & - & - & - \\
1 & -1 & -1 & 0 & 0 & \cdots & 0 & 0 & 0 & & & \cdots & 0 \\
0 & 1 & 0 & -1 & -1 & \cdots & 0 & 0 & 0 & & & & \vdots \\
\vdots & \vdots & \vdots & \vdots & \vdots & \vdots & \vdots & \vdots & \vdots & & & \ddots & \vdots \\
0 & 0 & 0 & 0 & 0 & \cdots & -1 & -1 & 1 & & & \cdots & 0
\end{bmatrix}$$

$$\mathbf{x}(t)=\begin{bmatrix} Q_1(t) \\ Q_2(t) \\ \vdots \\ Q_{22}(t) \\ P_1(t) \\ P_2(t) \\ \vdots \\ P_{14}(t) \end{bmatrix};\mathbf{y}(t)=\begin{bmatrix} P_A/R_1(t) \\ 0 \\ \vdots \\ -P_V/R_{22}(t) \\ - \\ 0 \\ 0 \\ \vdots \\ 0 \end{bmatrix}$$

from Eq. A5, we obtained N_s number of equations for all segments, and from Eq. A6, we obtained N_n number of equations for all nodes, discontinuous line separates both groups of equations. Which results in a $(N_s + N_n)$ square matrix, where N_s and N_n represent the number of segments and nodes in the network, respectively. $R_i(t)$ represent the vessels resistance at each segment i, P_A and P_V are the inlet and outlet pressures as shown in Table 1. The variables vector $\mathbf{x}(t)$ is formed with the CBF at each vessel segment and the pressures at each node.

Upon solving the system $\mathbf{A}(t)\mathbf{x}(t) = \mathbf{y}(t)$ at each time instant, $Q(t)$ and $P(t)$ values are obtained at all vessel segments and nodes, respectively. We use the computed blood flow values at each vessel segment to update hematocrit throughout the network by applying the phase separation effect and mass conservation at each bifurcation (Eq. A6-11), as described by Pries and Secomb, (2008). Indexes α, β and F denote both daughters and the feeding vessel at each bifurcation respectively. $F_H\alpha$ is the fraction of feeding vessel's RBCs entering daughter branch α. The updated hematocrit values are used to update viscosity and the resistance in all vessel segments. This process was repeated iteratively until convergence of the hematocrit values was achieved using a tolerance of 10^{-3}. Flow rate distribution in the vascular network is assumed to reach steady state at each time step Δt following a step change in a vessel's diameter, which we called the quasi-steady flow approximation.

As proposed in previous studies (Friston et al., 2000; Riera et al., 2004; Riera et al., 2007), the stimulus was generated via a vasoactive signal s that connects the neuronal activity $n(t)$, a relative variable and for now modeled as a Gaussian function, to diameter changes in the dilated arteriole that we denote with a subindex "a" (i.e., $D_a(t)$, $Q_a(t)$) (Eq. A12 and A13). $\varnothing$ denotes the relative diameter of the active arteriole. ε_{SF}, τ_s, and τ_f are parameters defined in the extended balloon model (Friston et al., 2000), representing the neurovascular strength and vascular dynamics time constants, respectively. We have extended this model to include limit saturation for the neurovascular signaling l_{NS} and the vessel dilation l_{VD}. Parameters ε_{SF} = 0.52, l_{SF} = 1 and l_{VD} = 0.25 were fixed to create a vasodilation compatible with those in the windkessel-based model (i.e., Eq. B5 and B6). Finally, the diameter of the active arteriole is then obtained using Eq. A14. Parameters $D_{a0} = D_a(t = 0)$ and $Q_{a0} = Q_a(t = 0)$ represent the resting/baseline values of the diameter and CBF in the active arteriole.

Appendix B. The parsimonious windkessel-based model

In this study, a parsimonious windkessel-based model was developed to explain ABS at a mesoscopic level. All model equations are shown in Table B1**.** Applying the second Kirchhoff's law and the windkessel theory (Mandeville et al., 1999), we obtained Eq. B1 and B2 to model the CBF dynamics in both regions (see deduction below). To represent transient changes in the post-capillary venous compliance, we used the extended viscoelastic extension model (Eq. B3) proposed by Zheng and Mayhew (2009). Eq. B4 models the relative variations in time of the viscoelastic compliance variable (a) that relates volume and windkessel flow. We employed the relationship proposed by Friston et al. (2000) to describe changes in vessel resistance as a function of the vasoactive signaling in the dilated lower-order arteriole (Eq. B5 and B6). A list summarizing the assumptions underlying this model is:

- Steady state representation of pressure–volume relationship (Mandeville et al., 1999)
- Viscoelastic compliance (Zheng and Mayhew, 2009)

Table B2
State variables of the parsimonious windkessel-based model.

State variables	Steady state/ baseline value
Relative neuronal activity ($\boldsymbol{n}$)	1
Vasoactive signal ($\boldsymbol{s}$)	0
Relative arteriole resistance ($\boldsymbol{r_a}$)	1
Relative cerebral blood volume (υ)	1
Relative CBF in the arteriole ($\boldsymbol{f_a}$)	1
Relative pressure to volume constant ($\boldsymbol{a}$)	1

Table B1
Set of equations used in the parsimonious windkessel-based model.

Model type	Equations	Variable	Reference
Hemodynamics	$L_A\boldsymbol{M}\frac{d\boldsymbol{f_a}}{dt} = \mathbf{1} - R_A\boldsymbol{M}\boldsymbol{f_a} - R_a^{(0)}\boldsymbol{R_a}\boldsymbol{f_a} - R_w^{(0)}\begin{bmatrix} v_1^{\beta}/a_1 \\ v_2^{\beta}/a_2 \end{bmatrix}$ [B1]	CBF	Appendix B
	$2R_A + R_a^{(0)} + R_w^{(0)} = 1$ [B2]	Normalized total network resistance	
	$\tau\frac{dv_{1,2}}{dt} = f_{a_{1,2}} - \frac{v_{1,2}^{\alpha+\beta}}{a_{1,2}}$ [B3]	CBV	Zheng and Mayhew, 2009
	$\tau_w\frac{da_{1,2}}{dt} = -a_{1,2} + e^{-b\frac{dv_{1,2}}{dt}}$ [B4]	Nonlinear viscoelastic	
Neurovascular coupling	$\frac{ds}{dt} = \varepsilon_{NS}(n-1) - \frac{s}{\tau_s} - \frac{(f_a-1)}{\tau_f}$ [B5]	Vasoactive signal	Friston et al., 2000
	$\frac{dr_a}{dt} = -r_a^2 s$ [B6]	Arteriole resistance	

Table B3
Parameters of the parsimonious windkessel-based model.

Parameter (units)	Symbol	Value	Range of possible values	Reference
Neurovascular coupling (input efficacy) (dimensionless)	ε_{WS}	0.28	[0.2–0.5]	(Friston, 2002)
Time constant of the vasoactive signal (s)	τ_s	1.1	[0.91–1.25]	
Autoregulation time constant (s)	τ_f	1.2		
Total tissue mean transit time (s)	τ	1.8	[1.2–2.4]	(Friston, 2002; Havlicek et al., 2015)
Diminished reserved volume exponent (dimensionless)	β	2		(Boas et al., 2008; Zheng and Mayhew, 2009)
Time constant of $\boldsymbol{a}$ (s)	τ_w	6.68		(Zheng and Mayhew, 2009)
Gain modeling influence of variation of CBV on $\boldsymbol{a}$ (s)	b	7.6		
Arterial inertial time constant (msec)	τ_A	1 Inferred		Section below
Feeding arteriole resistance (dimensionless)	R_A	estimated	[0.154–0.177]	See results
Basal daughter arterioles resistance (dimensionless)	R_a^0	estimated	[0.38–0.41]	See results

- Electrical equivalence of the vessel resistance and compliance is appropriate.
- An inductance with the resistance in series well describes blood inertia (Spronck et al., 2012).

Equation (B2) across all vessel resistance must be hold, thus, we can combine Eq. B1 and B2 in the form:

$$L_A\boldsymbol{M}\frac{d\boldsymbol{f_a}}{dt} = \boldsymbol{1} - R_A\boldsymbol{M}\boldsymbol{f_a} - R_a^{(0)}\boldsymbol{R_a}\boldsymbol{f_a} - \left(1 - 2R_A + R_a^{(0)}\right)\begin{bmatrix} v_1^{\beta}/a_1 \\ v_2^{\beta}/a_2 \end{bmatrix} \tag{B7}$$

$$\text{With } \boldsymbol{f_a} = \begin{bmatrix} f_{a_1} \\ f_{a_2} \end{bmatrix}, \boldsymbol{R_a} = \begin{bmatrix} r_a & 0 \\ 0 & 1 \end{bmatrix}, \boldsymbol{M} = \begin{bmatrix} 1 & 1 \\ 1 & 1 \end{bmatrix}, \text{and } \boldsymbol{1} = \begin{bmatrix} 1 \\ 1 \end{bmatrix}.$$

Resistance changes in the dilated arteriole compartment (r_a) are computed using (Eq. B6), which relates to neuronal activity through the vasoactive signal described using (Eq. B5). As **M** is a noninvertible matrix, our model is represented by a system of differential algebraic equations (DAE). Solutions were computed in MATLAB (MathWorks, Inc.) using "ode15s", a stiff differential equation solver suitable for DAE systems. All parameters and state variables used in this model are listed in Tables B2 and B3 respectively.

The inductance was determined using:

$$L = \frac{8\rho_B}{\pi D^2} l \tag{B8}$$

with $\rho_B = 1.056 g/ml$, the blood mass density. Then, computing the arteriole resistance using Hagen-Poiseuille equation (Eq. A5), the RL circuit time constant for the penetrating arteriole is defined as:

$$\tau_A = \frac{L_A}{R_A} = \frac{\eta D^2}{16\rho_B} \tag{B9}$$

As we accounted for small arterioles in our theoretical model (20–30 μm), inertial time effects can be neglected for these small diameters. Thus, we assumed it τ_A = 1 ms, same as the time step in our simulations.

Theoretical deduction of the equations for the CBF in the active/passive regions

Applying Kirchhoff 2nd law in the arterial and veins compartments in Fig. 3, we obtain:

(I) $L_A\frac{d(F_{a_1}+F_{a_2})}{dt} = P_0 - R_A(F_{a_1}+F_{a_2}) - R_{a_k}F_{a_k} - P_{w_k}$

(II) $0 = P_{w_k} - R_{w_k}F_{w_k}$

Applying windkessel theory and transforming absolute values into relative,

$$P_{w_k} = \frac{V_k^{\beta}}{A_k};\ \frac{R_{w_k}}{R_w^{(0)}} = \left(\frac{V_0}{V_k}\right)^{\alpha};\ f_{a_k} = \frac{F_{a_k}}{F_0};\ f_{wk} = \frac{F_{w_k}}{F_0};$$

$$r_{a_k} = \frac{R_{a_k}}{R_a^{(0)}};\ v_k = \frac{V_k}{V_0};\ a_k = \frac{A_k}{A_0}$$

Where $\propto = 2$

(I) $L_AF_0\frac{d(f_{a_1}+f_{a_2})}{dt} = P_0 - R_AF_0\left(f_{a_1}+f_{a_2}\right) - R_a^0rF_0f_{a_k} - \frac{v_k^{\beta}}{a_k}(A_0V_0^{-\beta})$

(II) $0 = \frac{v_k^{\beta}}{a_k}(A_0V_0^{-\beta}) - v_k^{-\alpha}R_w^{(0)}F_0f_{w_k}$

Writing these two equations in matrix form we obtain:

(I) $L_AF_0\boldsymbol{M}\frac{d\boldsymbol{f_a}}{dt} = P_0\begin{bmatrix}1\\1\end{bmatrix} - R_AF_0\boldsymbol{M}\boldsymbol{f_a} - R_a^{(0)}F_0\boldsymbol{R_a}\boldsymbol{f_a} - \boldsymbol{V}^{\beta}\boldsymbol{A}^{-1}C\begin{bmatrix}1\\1\end{bmatrix}$

(II) $0 = \boldsymbol{V}^{\beta}\boldsymbol{A}^{-1}C\begin{bmatrix}1\\1\end{bmatrix} - \boldsymbol{V}^{-\alpha}R_w^{(0)}F_0\boldsymbol{f_w}$

where:

$$\boldsymbol{f_a} = \begin{bmatrix} f_{a_1} \\ f_{a_2} \end{bmatrix}; \boldsymbol{f_w} = \begin{bmatrix} f_{w_1} \\ f_{w_2} \end{bmatrix}; \boldsymbol{R_a} = \begin{bmatrix} r_{a_1} & 0 \\ 0 & r_{a_2} \end{bmatrix};$$

$$\boldsymbol{V} = \begin{bmatrix} v_1 & 0 \\ 0 & v_2 \end{bmatrix}; \boldsymbol{A} = \begin{bmatrix} a_1 & 0 \\ 0 & a_2 \end{bmatrix}; \boldsymbol{M} = \begin{bmatrix} 1 & 1 \\ 1 & 1 \end{bmatrix}; C = (A_0V_0^{-\beta})$$

At baseline values, equation (I) simplifies like this:

$$C\begin{bmatrix}1\\1\end{bmatrix} = P_0\begin{bmatrix}1\\1\end{bmatrix} - \left(R_A\boldsymbol{M} + R_a^{(0)}\right)F_0\begin{bmatrix}1\\1\end{bmatrix}$$

Then, substituting this expression in (II) we obtain

$$F_0\begin{bmatrix}1\\1\end{bmatrix} = P_0\left(R_A\boldsymbol{M} + R_a^{(0)} + R_w^{(0)}\right)^{-1}\begin{bmatrix}1\\1\end{bmatrix}$$

$$\Rightarrow F_0 = P_0 diag\left\{P_0\left(R_A\boldsymbol{M} + R_a^{(0)} + R_w^{(0)}\right)^{-1}\right\}$$

Now, as we assume constant pressure, $P_0 = 1$ and $F_0 = \begin{bmatrix}1 & 0\\0 & 1\end{bmatrix}$, then we get:

$$2R_A + R_a^{(0)} + R_w^{(0)} = 1$$

Thus, $C = R_w^{(0)}$, and the substituting it into equations (I), we get:

$$L_A\boldsymbol{M}\frac{d\boldsymbol{f_a}}{dt} = \begin{bmatrix}1\\1\end{bmatrix} - (R_A\boldsymbol{M} + R_a^{(0)}\boldsymbol{R_a})\boldsymbol{f_a} - R_w^{(0)}\boldsymbol{V}^{\beta}\boldsymbol{A}^{-1}\begin{bmatrix}\boldsymbol{1}\\\boldsymbol{1}\end{bmatrix}$$

References

Bandettini, P., 2012. The BOLD plot thickens: sign- and layer-dependent hemodynamic changes with activation. Neuron 76 (3), 468–469. https://doi.org/10.1016/j.neuron.2012.10.026.

Bentzer, P., Grände, P.-O., 2017. Isolated brain trauma in cats triggers rapid onset of hypovolemia. Neurocrit. Care 26 (3), 450–456. https://doi.org/10.1007/s12028-016-0348-5.

Blockley, N.P., Griffeth, V.E., Buxton, R.B., 2012. A general analysis of calibrated BOLD methodology for measuring CMRO2 responses: comparison of a new

approach with existing methods. Neuroimage 60 (1), 279–289. https://doi.org/10.1016/j.neuroimage.2011.11.081.
Boas, D.A., Jones, S.R., Devor, A., Huppert, T.J., Dale, A.M., 2008. A vascular anatomical network model of the spatio-temporal response to brain activation. Neuroimage 40 (3), 1116–1129. https://doi.org/10.1016/j.neuroimage.2007.12.061.
Boorman, L., Kennerley, A.J., Johnston, D., Jones, M., Zheng, Y., Redgrave, P., Berwick, J., 2010. Negative blood oxygen level dependence in the rat: a model for investigating the role of suppression in neurovascular coupling. J. Neurosci. 30 (12), 4285–4294. https://doi.org/10.1523/JNEUROSCI.6063-09.2010.
de Courten-Myers, G.M., Yamaguchi, S., Wagner, K.R., Ting, P., Myers, R.E., 1985. Brain injury from marked hypoxia in cats: role of hypotension and hyperglycemia. Stroke 16 (6), 1016–1021. https://doi.org/10.1161/01.STR.16.6.1016.
Devor, A., Hillman, E.M.C., Tian, P., Waeber, C., Teng, I.C., Ruvinskaya, L., Shalinsky, M.H., Zhu, H., Haslinger, R.H., Narayanan, S.N., Ulbert, I., Dunn, A.K., Lo, E.H., Rosen, B.R., Dale, A.M., Kleinfeld, D., Boas, D.A., 2008. Stimulus-induced changes in blood flow and 2-deoxyglucose uptake dissociate in ipsilateral somatosensory cortex. J. Neurosci. 28 (53), 14347–14357. https://doi.org/10.1523/JNEUROSCI.4307-08.2008.
Driscoll, J.D., Shih, A.Y., Drew, P.J., Cauwenberghs, G., Kleinfeld, D., 2013. Two-photon imaging of blood flow in the rat cortex. Cold Spring Harbor Protocols 8, 759–767. https://doi.org/10.1101/pdb.prot076513.
Friston, K.J.J., 2002. Bayesian Estimation of Dynamical Systems: An Application to fMRI. Neuroimage 16, 513–530. https://doi.org/10.1006/nimg.2001.1044.
Friston, K.J., Mechelli, A., Turner, R., Price, C.J., 2000. Nonlinear responses in fMRI: the Balloon model, Volterra kernels, and other hemodynamics. Neuroimage 12 (4), 466–477. https://doi.org/10.1006/nimg.2000.0630.
Gagnon, L., Sakadžić, S., Lesage, F., Musacchia, J.J., Lefebvre, J., Fang, Q., Yücel, M.A., Evans, K.C., Mandeville, E.T., Cohen-Adad, J., Polimeni, J.R., 2015. Quantifying the microvascular origin of BOLD-fMRI from first principles with two-photon microscopy and an oxygen-sensitive nanoprobe. J. Neurosci. 35, 3663–3675. https://doi.org/10.1523/JNEUROSCI.3555-14.2015.
Goense, J., Merkle, H., Logothetis, N., 2012. High-resolution fMRI reveals laminar differences in neurovascular coupling between positive and negative BOLD responses. Neuron 76 (3), 629–639. https://doi.org/10.1016/j.neuron.2012.09.019.
Grubb, R.L., Raichle, M.E., Eichling, J.O., Ter-Pogossian, M.M., 1974. The effects of changes in PaCO2 cerebral blood volume, blood flow, and vascular mean transit time. Stroke 5 (5), 630–639. https://doi.org/10.1161/01.STR.5.5.630.
Gusnard, D.A., Raichle, M.E., 2001. Searching for a baseline: functional imaging and the resting human brain. Nat. Rev. Neurosci. 2 (10), 685–694. https://doi.org/10.1038/35094500.
Gutierrez, J., Rosoklija, G., Murray, J., Chon, C., Elkind, M.S.V., Goldman, J., Honig, L.S., Dwork, A.J., Morgello, S., Marshall, R.S., 2014. A quantitative perspective to the study of brain arterial remodeling of donors with and without HIV in the Brain Arterial Remodeling Study (BARS). Front. Physiol. 5, 56. https://doi.org/10.3389/fphys.2014.00056.
Harel, N., Lee, S.-P., Nagaoka, T., Kim, D.-S., Kim, S.-G., 2002. Origin of negative blood oxygenation level-dependent fMRI signals. J. Cereb. Blood Flow Metab. 22 (8), 908–917. https://doi.org/10.1097/00004647-200208000-00002.
Havlicek, M., Roebroeck, A., Friston, K., Gardumi, A., Ivanov, D., Uludag, K., 2015. Physiologically informed dynamic causal modeling of fMRI data. Neuroimage 122, 355–372. https://doi.org/10.1016/j.neuroimage.2015.07.078.
Hu, D., Huang, L., 2015. Negative hemodynamic response in the cortex: evidence opposing neuronal deactivation revealed via optical imaging and electrophysiological recording. J Neurophysiol 114, 2152–2161. https://doi.org/10.1152/jn.00246.2015.
Kannurpatti, S.S., Biswal, B.B., 2004. Negative functional response to sensory stimulation and its origins. J. Cereb. Blood Flow Metab. 24 (6), 703–712. https://doi.org/10.1097/01.WCB.0000121232.04853.46.
Kiyohara, Y., Fujishima, M., Ishitsuka, T., Tamaki, K., Sadoshima, S., Omae, T., 1985. Effects of hematocrit on brain metabolism in experimentally induced cerebral ischemia in spontaneously hypertensive rats (SHR). Stroke 16 (5), 835–840. https://doi.org/10.1161/01.STR.16.5.835.
Klingner, C.M., Hasler, C., Brodoehl, S., Witte, O.W., 2010. Dependence of the negative BOLD response on somatosensory stimulus intensity. Neuroimage 53 (1), 189–195. https://doi.org/10.1016/j.neuroimage.2010.05.087.
Lyons, D.G., Parpaleix, A., Roche, M., Charpak, S., 2016. Mapping oxygen concentration in the awake mouse brain. Elife. 5, 12024. 10.7554/eLife.12024.001.
Ma, Z., Cao, P., Sun, P., Lu, Z., Li, L., Chen, Y., Chai, X., 2017. Negative hemodynamic response without neuronal inhibition investigated by combining optical imaging and electrophysiological recording. Neurosci. Lett. 637, 161–167. https://doi.org/10.1016/j.neulet.2016.11.029.
Maggioni, E., Zucca, C., Reni, G., Cerutti, S., Triulzi, F.M., Bianchi, A.M., Arrigoni, F., 2016. Investigation of the electrophysiological correlates of negative BOLD response during intermittent photic stimulation: An EEG-fMRI study. Hum. Brain Mapp. 37 (6), 2247–2262. https://doi.org/10.1002/hbm.23170.
Mandeville, J.B., Marota, J.J.A., Ayata, C., Zaharchuk, G., Moskowitz, M.A., Rosen, B.R., Weisskoff, R.M., 1999. Evidence of a cerebrovascular postarteriole windkessel with delayed compliance. J. Cereb. Blood Flow Metab. 19 (6), 679–689. https://doi.org/10.1097/00004647-199906000-00012.
Matthews, P.M., Honey, G.D., Bullmore, E.T., 2006. Applications of fMRI in translational medicine and clinical practice. Nat Rev Neurosci. 7 (9), 732–744. https://doi.org/10.1038/nrn1929.
Moshkforoush, A., Balachandar, L., Moncion, C., Montejo, K.A., Riera, J., Berry, H., 2021. Unraveling ChR2-driven stochastic Ca2+ dynamics in astrocytes: a call for new interventional paradigms. PLoS Comput. Biol. 17 (2), e1008648.
Muizelaar, J.P., Bouma, G.J., Levasseur, J.E., Kontos, H.A., 1992. Effect of hematocrit variations on cerebral blood flow and basilar artery diameter in vivo. Am. J. Physiol.-Heart Circul. Physiol. 262 (4), H949–H954. https://doi.org/10.1152/ajpheart.1992.262.4.H949.
Nagaoka, T., Zhao, F., Wang, P., Harel, N., Kennan, R.P., Ogawa, S., Kim, S.-G., 2006. Increases in oxygen consumption without cerebral blood volume change during visual stimulation under hypotension condition. J. Cereb. Blood Flow. Metab. 26 (8), 1043–1051. https://doi.org/10.1038/sj.jcbfm.9600251.
Ogawa, S., Menon, R.S., Kim, S.-G., Ugurbil, K., 1998. On the characteristics of functional magnetic resonance imaging of the brain. Annu. Rev. Biophys. Biomol. Struct. 27 (1), 447–474. https://doi.org/10.1146/annurev.biophys.27.1.447.
Pries, A.R., Secomb, T.W., 2005. Microvascular blood viscosity in vivo and the endothelial surface layer. Am. J. Physiol.-Heart Circul. Physiol. 289 (6), H2657–H2664. https://doi.org/10.1152/ajpheart.00297.2005.
Pries, A.R., Secomb, T.W., 2008. Blood flow in microvascular networks. In: Microcirculation. Elsevier, pp. 3–36.
Qian, B., Rudy, R.F., Cai, T., Du, R., 2018. Cerebral artery diameter in inbred mice varies as a function of strain. Front. Neuroanat. 12, 10. https://doi.org/10.3389/fnana.2018.00010.
Raichle, M.E., MacLeod, A.M., Snyder, A.Z., Powers, W.J., Gusnard, D.A., Shulman, G.L., 2001. A default mode of brain function. Proc. Natl. Acad. Sci. 98 (2), 676–682. https://doi.org/10.1073/pnas.98.2.676.
Reina-De La Torre, F., Rodriguez-Baeza, A., Sahuquillo-Barris, J., 1998. Morphological characteristics and distribution pattern of the arterial vessels in human cerebral cortex: a scanning electron microscope study. Anatom. Record. 251 (1), 87–96. https://doi.org/10.1002/(SICI)1097-0185(199805)251:1<87::AID-AR14>3.0.CO;2-7.
Riera, J., Bosch, J., Yamashita, O., Kawashima, R., Sadato, N., Okada, T., Ozaki, T., 2004. fMRI activation maps based on the NN-ARx model. Neuroimage 23 (2), 680–697. https://doi.org/10.1016/j.neuroimage.2004.06.039.
Riera, J.J., Jimenez, J.C., Wan, X., Kawashima, R., Ozaki, T., 2007. Nonlinear local electrovascular coupling. II: from data to neuronal masses. Hum. Brain Mapp. 28 (4), 335–354. https://doi.org/10.1002/hbm.20278.
Riera, J.J., Sumiyoshi, A., 2010. Brain oscillations: ideal scenery to understand the neurovascular coupling. Curr. Opin. Neurol. 23, 374–381. https://doi.org/10.1097/WCO.0b013e32833b769f.
Rosen, B.R., Buckner, R.L., Dale, A.M., 1998. Event-related functional MRI: Past, present, and future. Proc. Natl. Acad. Sci. U.S.A. 95 (3), 773–780. https://doi.org/10.1073/pnas.95.3.773.
Schäfer, K., Blankenburg, F., Kupers, R., Grüner, J.M., Law, I., Lauritzen, M., Larsson, H.B.W., 2012. Negative BOLD signal changes in ipsilateral primary somatosensory cortex are associated with perfusion decreases and behavioral evidence for functional inhibition. Neuroimage 59 (4), 3119–3127. https://doi.org/10.1016/j.neuroimage.2011.11.085.
Schridde, U., Khubchandani, M., Motelow, J.E., Sanganahalli, B.G., Hyder, F., Blumenfeld, H., 2008. Negative BOLD with large increases in neuronal activity. Cereb. Cortex. 18, 1814–1827. https://doi.org/10.1093/cercor/bhm208.
Shih, Y.-Y.-I., Chen, C.-C.-V., Shyu, B.-C., Lin, Z.-J., Chiang, Y.-C., Jaw, F.-S., Chen, Y.-Y., Chang, C., 2009. A new scenario for negative functional magnetic resonance imaging signals: endogenous neurotransmission. J. Neurosci. 29 (10), 3036–3044. https://doi.org/10.1523/JNEUROSCI.3447-08.2009.
Smith, A.T., Williams, A.L., Singh, K.D., 2004. Negative BOLD in the visual cortex: evidence against blood stealing. Hum. Brain Mapp. 21 (4), 213–220. https://doi.org/10.1002/hbm.20017.
Smith, A.F., Doyeux, V., Berg, M., Peyrounette, M., Haft-Javaherian, M., Larue, A.-E., Slater, J.H., Lauwers, F., Blinder, P., Tsai, P., Kleinfeld, D., Schaffer, C.B., Nishimura, N., Davit, Y., Lorthois, S., 2019. Brain capillary networks across species: a few simple organizational requirements are sufficient to reproduce both structure and function. Front. Physiol. 10.
Shmuel, A., Augath, M., Oeltermann, A., Logothetis, N.K., 2006. Negative functional MRI response correlates with decreases in neuronal activity in monkey visual area V1. Nat Neurosci 9, 569–577. https://doi.org/10.1038/nn1675.
Shmuel, A., Yacoub, E., Pfeuffer, J., Van de Moortele, P.-F., Adriany, G., Hu, X., Ugurbil, K., 2002. Sustained negative BOLD, blood flow and oxygen consumption response and its coupling to the positive response in the human brain. Neuron 36 (6), 1195–1210. https://doi.org/10.1016/S0896-6273(02)01061-9.
Song, Y., Torres, R.A., Garcia, S., Frometa, Y., Bae, J., Deshmukh, A., Lin, W.-C., Zheng, Y., Riera, J.J., 2016. Dysfunction of neurovascular/metabolic coupling in chronic focal epilepsy. IEEE Trans. Biomed. Eng. 63 (1), 97–110. https://doi.org/10.1109/TBME.2015.2461496.
Spronck, B., Martens, E.G.H.J., Gommer, E.D., van de Vosse, F.N., 2012. A lumped parameter model of cerebral blood flow control combining cerebral autoregulation and neurovascular coupling. Am. J. Physiol.-Heart Circul. Physiol. 303 (9), H1143–H1153. https://doi.org/10.1152/ajpheart.00303.2012.
Sten, S., Lundengård, K., Witt, S.T., Cedersund, G., Elinder, F., Engström, M., 2017. Neural inhibition can explain negative BOLD responses: a mechanistic

modelling and fMRI study. Neuroimage 158, 219–231. https://doi.org/10.1016/j.neuroimage.2017.07.002.

Suarez, A., Valdes-Hernandez, P.A., Bernal, B., Dunoyer C., Ming Khoo, H., von-Ellenrieder, N., Bosch-Bayard, J., Riera, J. Identification of negative BOLD responses in epilepsy using windkessel models. Front. Neurol., under review, 2021.

Yang, Z., Craddock, R.C., Milham, M.P., 2015. Impact of hematocrit on measurements of the intrinsic brain. Front. Neurosci. 8, 452. https://doi.org/10.3389/fnins.2014.00452.

Zheng, Y., Mayhew, J., 2009. A time-invariant visco-elastic windkessel model relating blood flow and blood volume. Neuroimage 47 (4), 1371–1380. https://doi.org/10.1016/j.neuroimage.2009.04.022.